

FULL PAPER

# Cation distribution and diffusion-path topologies of A-site-deficient perovskite $\text{Li}_x\text{La}_{(1-x)/3}\text{NbO}_3$

Naoto Kitamura<sup>1,2,†</sup>, Yizhong Tang<sup>1</sup>, Koji Kimura<sup>3</sup>, Ippei Obayashi<sup>4</sup>, Yohei Onodera<sup>2</sup>, Ken Nakashima<sup>5</sup>, Chiaki Ishibashi<sup>1</sup>, Yasushi Idemoto<sup>1</sup> and Koichi Hayashi<sup>3</sup>

<sup>1</sup>Department of Pure and Applied Chemistry, Faculty of Science and Technology, Tokyo University of Science, 2641 Yamazaki, Noda, Chiba 278–8510, Japan

<sup>2</sup>Center for Basic Research on Materials, National Institute for Materials Science, 1–2–1 Sengen, Tsukuba, Ibaraki 305–0047, Japan

<sup>3</sup>Department of Physical Science and Engineering, Nagoya Institute of Technology, Gokiso, Showa, Nagoya 466–8555, Japan

<sup>4</sup>Center for Artificial Intelligence and Mathematical Data Science, Okayama University, Okayama 700–8530, Japan

<sup>5</sup>Faculty of Materials for Energy, Shimane University, 1060 Nishikawatsu-cho, Matsue 690–0823, Japan

$\text{Li}_x\text{La}_{(1-x)/3}\text{NbO}_3$  with an A-site-deficient perovskite structure was investigated with a focus on the relationship between its atomic configuration and  $\text{Li}^+$  diffusion properties. To this end, total scattering (diffraction) measurements were performed, and then reverse Monte Carlo modeling using the data was employed to construct the atomic configuration. The results suggest that the partial occupancy of La in the La-poor layer facilitate  $\text{Li}^+$  diffusion across the layer owing to the volume contraction. Furthermore, topological analyses conducted via persistent homology using the constructed atomic configuration indicate that a large fourfold ring formed by Nb and O is one of the reasons for superior  $\text{Li}^+$  diffusion in  $\text{Li}_x\text{La}_{(1-x)/3}\text{NbO}_3$ .

Key-words : A-site-deficient perovskite,  $\text{Li}^+$  conduction, Total scattering, Local structure, Persistent homology

[Received May 27, 2025; Accepted October 7, 2025; Published online November 12, 2025]

## 1. Introduction

In recent years, the realization of low-carbon societies through a reduction in  $\text{CO}_2$  emissions has become an urgent need, and renewable energy resources such as solar energy need to be effectively harnessed. Achieving this goal requires the widespread use of large rechargeable batteries for storing renewable energy, and lithium-ion batteries—which have been used as a power source for small portable devices—are expected to be applied even to larger systems.<sup>1,2)</sup> However, serious safety issues exist in the case of large lithium-ion batteries; thus, the development of batteries carrying minimized risks of ignition has been promoted in the last few decades, such as all-solid-state lithium-ion batteries that use solid electrolytes instead of liquid ones. Oxides possessing a perovskite structure ( $\text{ABO}_3$ -type structure) are regarded as candidates for the solid electrolyte; in this regard,  $\text{Li}_x\text{La}_{(1-x)/3}\text{NbO}_3$  with A-site vacancies (LLNO) showing remarkable  $\text{Li}^+$  conduction has been extensively studied.<sup>3–14)</sup> Moreover, the capability of LLNO for allowing insertion and deinsertion of lithium ions at around 1.5 V vs.  $\text{Li}/\text{Li}^+$  has recently

attracted significant attention, and some studies have focused on LLNO as a negative-electrode (anode) material that can replace carbon materials used in commercialized lithium-ion batteries.<sup>15,16)</sup> Given this background, one of the most important focus areas in the field of rechargeable batteries is the elucidation of the ion diffusion mechanism in materials with an A-site-deficient perovskite structure.

As is well known, ion diffusion in crystals is generally closely related to the atomic configurations. In the case of perovskite-type oxides such as LLNO that partially lack A-site cations, lithium ions are thought to diffuse via vacancies at the A sites.<sup>6,14)</sup> Therefore, the distributions of  $\text{Li}^+$ ,  $\text{La}^{3+}$ , and vacancies at the A sites in LLNO are thought to have a considerable influence on the ease of  $\text{Li}^+$  diffusion. However, because these distributions often do not show translational symmetry, conventional analyses of Bragg peaks in powder X-ray diffraction (XRD) patterns, i.e., Rietveld refinement, may neglect important structural information. Indeed, some studies on LLNO have examined the atomic configuration (La distribution) in a selected area via electron microscopy<sup>6,8,12,14)</sup> and also discussed the relationship between the configuration and ionic conduction properties using computational methods.<sup>8,11,13)</sup> However, the atomic configuration of the whole crystal has not been sufficiently elucidated experimentally.

As one of the experimental methods to fill this gap in literature, our previous work focused on X-ray fluores-

<sup>†</sup> Corresponding author: N. Kitamura; E-mail: [naotok@rs.tus.ac.jp](mailto:naotok@rs.tus.ac.jp)

<sup>‡</sup> Preface for this article: DOI <https://doi.org/10.2109/jcersj2.134.P4-1>

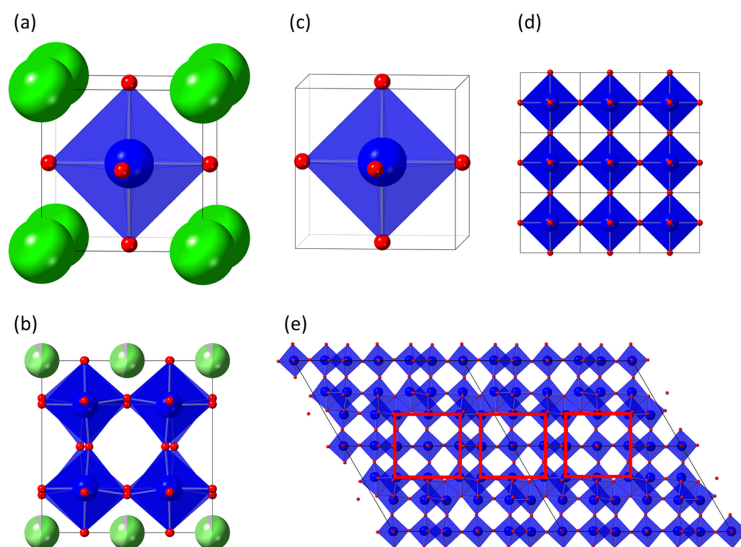


**Fig. 1.** Schematic illustrations of perovskite-related structures. (a) Perovskite structure ( $\text{ABO}_3$ ), (b) A-site-deficient perovskite structure [ $\text{Li}_x\text{La}_{(1-x)/3}\text{NbO}_3$ ], (c)  $\text{ReO}_3$ -type structure ( $\text{BO}_3$  with corner-sharing  $\text{BO}_6$  network), (d) structure of  $\text{ReO}_3$ -type  $3 \times 3 \times 3$  super cell, and (e) Wadsley–Roth phase  $\text{TiNb}_2\text{O}_7$  with  $3 \times 3 \times 3$  corner-sharing networks (perovskite blocks) represented by red squares. Color code: A atom, green; B atom, blue; and O, red.

cence holography (XFH), which records the modulation of the fluorescent X-ray intensity emitted from a target atom by surrounding atoms.<sup>17,18)</sup> We applied XFH to a LLNO single crystal grown by the Czochralski method to investigate the distribution of La within the crystal.<sup>10,19)</sup> Although LLNO has been believed to have essentially a layered structure with alternatively stacked La-occupied and La-deficient layers, as shown in **Fig. 1**,<sup>3)</sup> the XFH technique successfully demonstrated that a certain amount of La existed in the La-deficient layer, at least in the single crystal, and it also indicated the presence of column-like La arrangements locally.<sup>19)</sup> Moreover, the analyses also suggested that La migrating into the defective layer contributed to the enhanced  $\text{Li}^+$  conduction across this layer. However, as discussing the atomic positions in detail based solely on XFH is very difficult, the relationship between the atomic configuration and  $\text{Li}^+$  diffusion is not well understood.

Therefore, this study involves construction of the three-dimensional atomic configuration of LLNO with an A-site-deficient perovskite structure and a discussion of its correlation with  $\text{Li}^+$  diffusion. To this end, we performed neutron total scattering measurement experiments on LLNO along with reverse Monte Carlo (RMC) modeling using the obtained data<sup>20,21)</sup> to examine the distribution of Li, La, and vacancies in the A-site and local environments around them. Furthermore, as it is known that insertion and deinsertion of  $\text{Li}^+$  is possible in  $\text{TiNb}_2\text{O}_7$  in the Wadsley–Roth phase, the structure of which partially contains perovskite blocks without cations at the A site (Fig. 1),<sup>22–26)</sup> we compared the shape of the perovskite blocks in  $\text{TiNb}_2\text{O}_7$  with that of the blocks in LLNO. Based on the results thereof, we discuss the influence of the perovskite block shape on  $\text{Li}^+$  diffusion.

## 2. Experimental

### 2.1 Synthesis

LLNO with  $x = 0.20$ , i.e.,  $\text{Li}_{0.2}\text{La}_{0.8/3}\text{NbO}_3$ , was synthesized via a conventional solid-state reaction method employing  $\text{LaNb}_3\text{O}_9$  and  $\text{LiNbO}_3$  as per previous literature.<sup>7)</sup> To prepare  $\text{LaNb}_3\text{O}_9$ , a mixture of  $\text{La}_2\text{O}_3$  and  $\text{Nb}_2\text{O}_5$  with a molar ratio of 1:3 was calcined at 1100 °C for 3 h and then sintered at 1200 °C for 12 h.  $\text{LiNbO}_3$  was prepared by sintering a mixture of  $\text{Li}_2\text{CO}_3$  and  $\text{Nb}_2\text{O}_5$  at 1000 °C for 5 h. The synthesized  $\text{LaNb}_3\text{O}_9$  and  $\text{LiNbO}_3$  were then mixed in an appropriate proportion and sintered at 1200 °C for 12 h. As a reference material, LLNO with  $x = 0.10$  was also prepared in the same manner.

### 2.2 Average and local structure analyses

A phase of the synthesized LLNO was identified via a synchrotron XRD pattern measured using BL19B2 installed at SPring-8 ( $\lambda = 0.5 \text{ \AA}$ ), following which Rietveld refinement employing the pattern was conducted using the Rietan-FP program.<sup>27)</sup>

To uncover the distributions of Li, La, and vacancies at the A-sites and local environments around them, neutron total scattering measurements were performed using NOVA installed at J-PARC. The scattering pattern was collected with a 45° bank, and then a Faber–Ziman structure factor,  $S(Q)$ , was obtained from the pattern using calibration data (background, V-rod, and V-Ni alloy can). The reduced pair distribution function,  $G(r)$ , was also derived from  $S(Q)$  using a Fourier transform relation.<sup>28)</sup>

To construct a snapshot of the atomic configuration of LLNO, RMC modeling simultaneously employing the total scattering data and Bragg profile was performed using RMCProfile code.<sup>29)</sup> For the modeling,  $S(Q)$  was con-

volved by considering a simulation-box size to extract information on the local structures, and the convolved  $S(Q)$  is referred to as  $S_{\text{box}}(Q)$  hereafter. An initial simulation box with 964 atoms and 116 transparent atoms for the vacant positions was created from the unit cell refined using the aforementioned Rietveld analysis. For the RMC modeling, the Li, La, and vacancies were swapped to optimize the cation and vacancy distributions; moreover, bond-valence-sum (BVS) constraints, using bond valence parameters of 1.466, 2.172, and 1.911 ( $B = 0.37$ ) for  $\text{Li}^+ - \text{O}^{2-}$ ,  $\text{La}^{3+} - \text{O}^{2-}$ , and  $\text{Nb}^{5+} - \text{O}^{2-}$ , respectively, were applied to maintain appropriate nearest-neighbor distances.<sup>30,31)</sup> The polyhedral volumes of  $\text{LiO}_{12}$  and  $\text{LaO}_{12}$  were estimated from the obtained snapshot of the atomic configuration. For elucidation of the possible  $\text{Li}^+$  positions, which are supposed to reflect the  $\text{Li}^+$  diffusion paths, distribution of BVS within the atomic configuration was also calculated using PyAbstantia code.<sup>32)</sup> For obtaining a deeper understanding of the configuration, a topological analysis was conducted, as described in the following subsection.

### 2.3 Topological analysis

According to existing literature on  $\text{TiNb}_2\text{O}_7$  containing perovskite blocks in its crystal, the ring shape formed by a corner-sharing  $\text{BO}_6$  octahedral network has a significant influence on  $\text{Li}^+$  diffusion.<sup>26)</sup> Therefore, for evaluating ring size and shape, ring size distributions were calculated using the R.I.N.G.S. code<sup>33)</sup> and an analysis based on persistent homology (PH) was performed using HomCloud code.<sup>34,35)</sup> The latter analysis returns topological features, such as information of rings and voids (cavities), from three-dimensional atomic configurations, and these features are presented in two-dimensional format, i.e., a persistence diagram (PD) (Fig. S1). In the analysis, a sphere was placed at each atomic position, and its radius was increased from 0 to a larger value. The “birth” represents the radius at which a new ring or void is generated, and the “death” represents the radius at which this ring or void is annihilated. All pairs of birth (Å) and death (Å) are plotted in the PD. Therefore, the PD provides information on the sizes and shapes of the rings and voids. In other words, it enables us to investigate the sizes and shapes of possible  $\text{Li}^+$  diffusion pathways in  $\text{Li}^+$ -conducting materials. In this study, we developed the one-dimensional PD (PD1) to obtain information on the ring shape formed by the  $\text{BO}_6$  octahedral network. Further details on the PH analysis are described in existing literature.<sup>34,36)</sup>

## 3. Results and discussion

### 3.1 Average structure

Prior to examining the local structure of LLNO with  $x = 0.20$ , we identified the phase of LLNO and performed Rietveld analysis to refine the average structure. **Figure 2** shows the analytical pattern obtained using synchrotron XRD as well as the refined average structure, and Table S1 shows the refined structural parameters. Additionally, an enlarged view of the diffraction pattern around  $d = 1.38 \text{ Å}$  is also presented in Fig. S2. In the XRD pattern, all Bragg

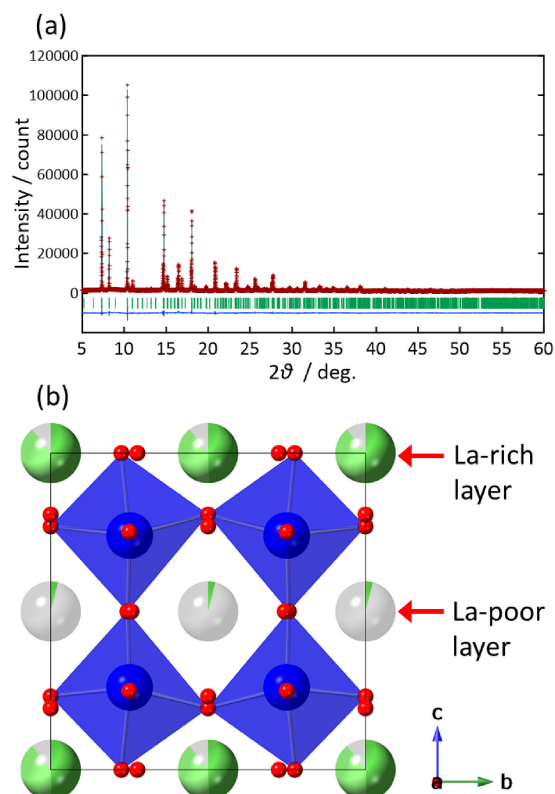


**Fig. 2.** Average structure analysis of LLNO ( $x = 0.20$ ). (a) Rietveld refinement pattern (X-ray) and (b) refined average structure. Color code: Li, light green; La, green; Nb, blue; and O, red.

peaks can be assigned to the perovskite structure with A-site defects. Typically, LLNO around  $x = 0.20$  is considered to be tetragonal, and the two prominent peaks observed in Fig. S2 are assigned to the (024) and (220) planes of the tetragonal structure.<sup>3)</sup> However, under the synthesis conditions employed in this study, the lower-angle peak shown in Fig. S2 broadened, indicating a slight change toward an orthorhombic structure. Therefore, Rietveld analysis was performed herein assuming an orthorhombic structure, and good fitting was resultantly obtained, as shown in Fig. 2(a). Furthermore, while the reliability factor,  $R_F$ , was 4.19 % when we assumed that La did not exist at the  $4h$  site in the La-deficient layer (this result is now shown), the  $R_F$  was 4.05 % when we assumed that La could occupy this layer (Table S1). That is, the  $R_F$  value decreased slightly under the latter assumption, and the La occupancy was 0.038. This trend is consistent with the results of previous studies employing XFH<sup>19)</sup> and scanning transmission electron microscopy (STEM).<sup>6,8)</sup> Therefore, hereafter, we refer to the layer as not “La-deficient” but “La-poor.”

To gain further insight into the structural differences between the La-rich and La-poor layers, we calculated the volumes of the  $\text{AO}_{12}$  polyhedra formed at the two A-sites ( $4g$  and  $4h$  sites shown in Table S1). The results demonstrate that the volume in the La-rich layer was  $46.78 \text{ Å}^3$ , while that in the La-poor layer was  $54.47 \text{ Å}^3$ . Previous studies have reported that  $\text{Li}^+$  diffuses predominantly

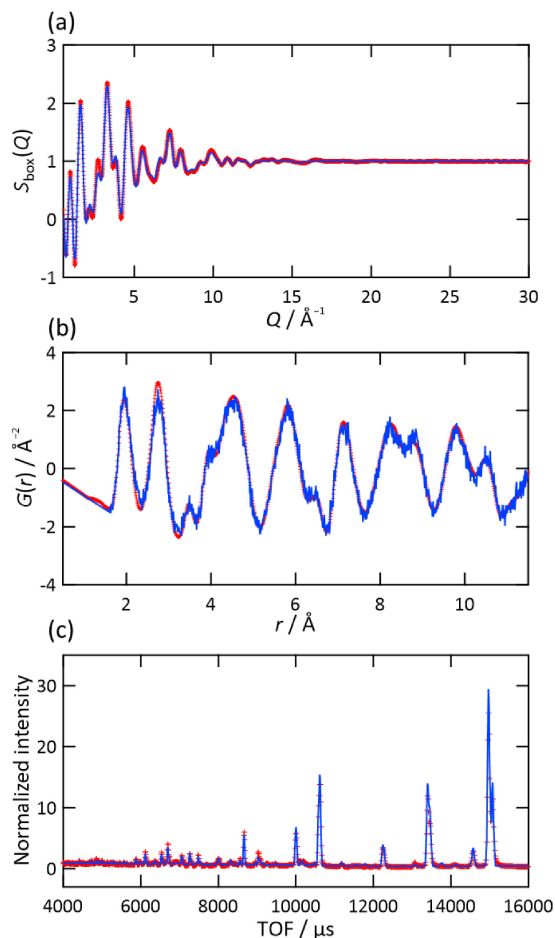


**Fig. 3.** RMC modeling of LLNO. (a) Convolved neutron structure factor, (b) neutron reduced pair distribution function, and (c) neutron Bragg profile. The red plus marks and blue solid line represent the experimental data and RMC model, respectively.

through the La-rich layer; thus, the electrical conductivity of  $\text{Li}^+$  along the  $c$ -axis is lower than that along the other directions.<sup>6,8–10,13</sup> Considering these results, the volume of the La-poor layer seems to be too large for accommodating  $\text{Li}^+$  diffusion.

### 3.2 Local structure

Because average structure analysis cannot distinguish Li, La, and vacancies at the A-sites, RMC modeling was performed using the total scattering data in addition to the Bragg profile. **Figure 3** shows the fitting patterns obtained via the RMC modeling, and **Fig. 4(a)** shows the obtained atomic configuration. As shown in Fig. 3, this atomic configuration can reproduce not only the Bragg profile but also the total scattering data well. Similar to the Rietveld analysis result described earlier, the RMC modeling result indicates that part of the La occupies the La-poor layer [Fig. 4(a)].

To gain further detailed insight into the distribution of  $\text{Li}^+$ ,  $\text{La}^{3+}$ , and vacancies, we investigated the atoms in the La-rich layers surrounding La in the La-poor layer (Fig. S3). We found that, on average, 7.7 Li and 8.7 La atoms surround La in the La-poor layer. Considering the

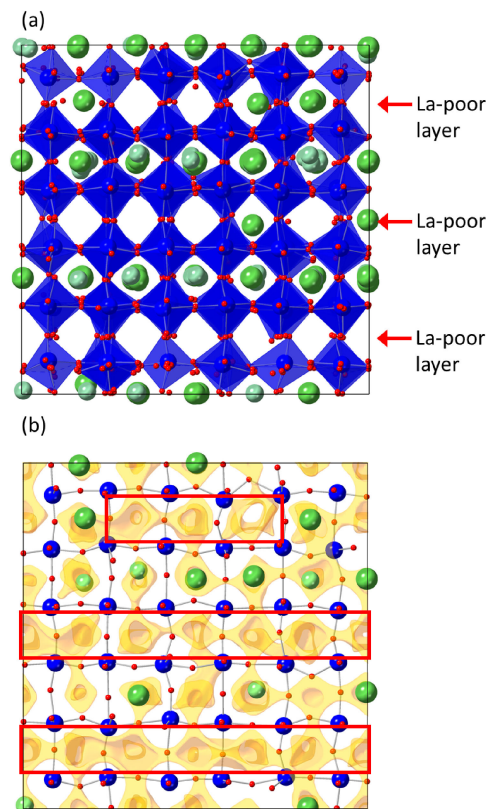


**Fig. 4.** Atomic configuration of LLNO. (a) Snapshot of atomic configuration obtained via the RMC modeling. The color code is as in Fig. 2. (b) BVS mapping in the atomic configuration. The red rectangles represent the mapping around vacant spaces in the La-poor layers.

**Table 1.** Polyhedral volumes of  $\text{LiO}_{12}$  and  $\text{LaO}_{12}$  in La-rich and poor layers along with average  $\text{AO}_{12}$  volumes estimated from average structure

Polyhedron	Layer	Volume/ $\text{\AA}^3$	Volume estimated from average structure/ $\text{\AA}^3$
$\text{LiO}_{12}$	La-rich	47.4	46.8
$\text{LaO}_{12}$		47.2	
$\text{LaO}_{12}$	La-poor	49.9	54.5

local electroneutrality condition,  $\text{La}^{3+}$  is less likely to exist around  $\text{La}^{3+}$  than around  $\text{Li}^+$ , but such a trend cannot be observed at the scale of the surrounding atoms mentioned above. Because our XFH analysis revealed La columnar arrangements in the case of a single crystal of LLNO,<sup>19</sup> La might tend to exist relatively easily around La in the A-site-deficient perovskite LLNO.

Using the BVS mapping obtained from the snapshot of the atomic configuration, we also examined the spaces where  $\text{Li}^+$  is likely to exist, and the results are shown in yellow in Fig. 4(b). As shown in this figure, we map the regions where the BVS values range from 0.7 to 1.3. In addition, **Table 1** shows the volumes of  $\text{LiO}_{12}$  and  $\text{LaO}_{12}$  polyhedra in the La-rich and La-poor layers, along with the average  $\text{AO}_{12}$  volumes in both layers estimated from the average structure. It is apparent from the BVS mapping



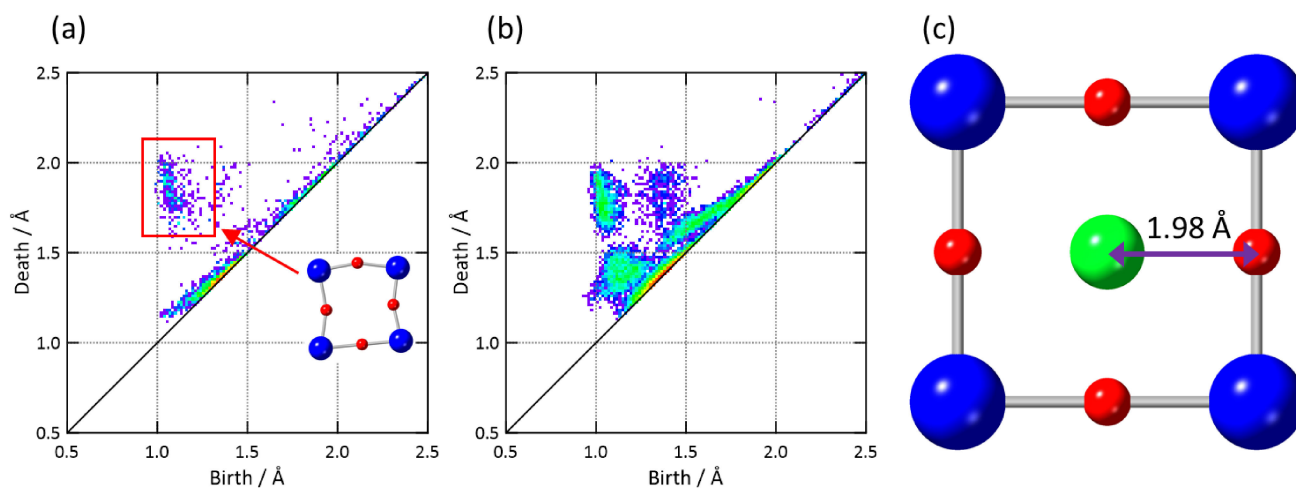


**Fig. 5.** Analysis using persistent homology for a topological dimensionality of 1. (a) Nb- and O-centric PD for LLNO. (b) PD for TiNb<sub>2</sub>O<sub>7</sub>. Reproduced with permission from Ref. 26). (c) Schematic illustration of ideal bottleneck for Li<sup>+</sup> diffusion (O<sub>4</sub> window).

that Li<sup>+</sup> does not preferentially exist at the center of the voids, particularly in the La-poor layers, as indicated by the red rectangles. This suggests that the La-poor layer is less suitable for Li<sup>+</sup> conduction compared to the La-rich layer although Li<sup>+</sup> can conduct through the La-poor layer. Indeed, conductivity measurements using a single crystal of LLNO demonstrated that the conductivity in the layer-stacking direction, i.e., *c*-axis direction is lower than in the *ab* plane.<sup>10)</sup> This difference in the Li<sup>+</sup> conduction is considered to be due to the significantly larger volume of the La-poor layer, as determined by Rietveld refinement (Table 1), compared to the volume of LiO<sub>12</sub>: that is, the large volume of the La-poor layer may be unsuitable for Li<sup>+</sup> conduction.

It is also noteworthy that the volume of LaO<sub>12</sub> in the La-poor layer is much smaller than that obtained via the Rietveld refinement, suggesting that the volume of the La-poor layer is decreased by the partial occupancy of La. To confirm this, we also performed the Rietveld refinement for LLNO with *x* = 0.10 (Fig. S4 and Table S2). Comparing the refinement results for the samples with different *x* (Table S3), it is found that the volume of the La-poor layer decreases as the occupancy of La in the layer increases. Since the volume of the La-poor layer is too large for Li<sup>+</sup> conduction basically as mentioned above, these analytical results suggest that Li<sup>+</sup> diffusion across the La-poor layer becomes easily owing to the volume contraction by the partial occupancy of La. Indeed, previous studies have indicated through molecular dynamics simulations that Li<sup>+</sup> conduction along the *c*-axis improves when La partially occupies the La-poor layer.<sup>8)</sup>

### 3.3 Topologies of perovskite blocks

In recent years, our studies have focused on compounds with the Wadsley–Roth phase containing perovskite blocks in the crystals, and we have investigated the relationship between the atomic configuration and negative-electrode properties.<sup>26,37,38)</sup> In particular, we have per-

formed a detailed topological analysis based on PH for the atomic configuration of TiNb<sub>2</sub>O<sub>7</sub>,<sup>26)</sup> revealing that the shape of the octahedral network formed by corner-sharing BO<sub>6</sub> (TiO<sub>6</sub> and NbO<sub>6</sub>) significantly influences the electrode properties. For the LLNO studied herein, Li<sup>+</sup> is thought to diffuse through free space in the corner-sharing octahedral network formed by NbO<sub>6</sub>. Considering the structural similarity between LLNO and TiNb<sub>2</sub>O<sub>7</sub>, we herein applied this analysis to the atomic configuration of LLNO and compared the shape of the BO<sub>6</sub> (NbO<sub>6</sub>) network in LLNO with that in TiNb<sub>2</sub>O<sub>7</sub> to reveal the reason for excellent lithium-ion diffusion in LLNO.

**Figure 5** shows the one-dimensional persistent diagram (PD) of this network in LLNO, along with that of TiNb<sub>2</sub>O<sub>7</sub>.<sup>26)</sup> In our analysis, Li and La were not considered for examining only the shape of the octahedral network; that is, this figure only shows the Nb- and O-centric PD. As clearly shown, many plots are concentrated along the diagonal line, where the birth and death values are rather close. As previously reported for TiNb<sub>2</sub>O<sub>7</sub>, these plots can be attributed to triangles within NbO<sub>6</sub> and are thus not related to the Li<sup>+</sup> diffusion pathway.<sup>26)</sup> Contrastingly, plots with a birth value around 1.1 Å and death value around 1.9 Å are supposed to be attributed to larger rings. According to ring analysis based on a primitive method,<sup>39)</sup> there are fourfold rings formed by four Nb and four O atoms, and sixfold rings detected due to the slight difference in the Nb–O distance within the fourfold rings (Fig. S5). Therefore, the plots can be basically originated from the fourfold ring, as shown in Fig. 5(a). Considering the fact that Li<sup>+</sup> diffuses through the corner-sharing NbO<sub>6</sub> network, this fourfold ring (which is the O<sub>4</sub> window) is regarded as a bottleneck for Li<sup>+</sup> diffusion.<sup>6,13)</sup> Indeed, in the perovskite block of TiNb<sub>2</sub>O<sub>7</sub>, the distortion of the fourfold ring is considered to hinder Li<sup>+</sup> diffusion, leading to poor electrode properties.<sup>26)</sup>

Considering these factors, we performed investigations for the ideal size and shape of the fourfold ring based on

the BVS for  $\text{Li}^+$  at the center of the ring, and the result shows that the BVS at the center becomes +1 when the distance between the center and oxygen is ca. 1.98 Å in the case of the square fourfold ring [Fig. 5(c)]. This corresponds to the birth value of 0.99 Å and death value of 1.98 Å. When this result is compared with that in Figs. 5(a) and 5(b), the death values of the fourfold rings in LLNO tend to be larger than those in  $\text{TiNb}_2\text{O}_7$  and close to the ideal value (1.98 Å) although they are distributed in an area smaller than the ideal value, probably due to displacements of Nb.<sup>6,13)</sup>

According to previous studies which determined diffusion coefficients of  $\text{Li}^+$  via a galvanostatic intermittent titration technique (GITT),<sup>16,40)</sup> the diffusion coefficients in LLNO-based materials are approximately  $2.5 \times 10^{-12}$  and  $9.5 \times 10^{-10} \text{ cm}^2 \text{ s}^{-1}$  for  $\text{Li}^+$  insertion and deinsertion, respectively, and appear to be much higher than that in  $\text{TiNb}_2\text{O}_7$ , which ranges from  $1.2 \times 10^{-14}$  to  $1.4 \times 10^{-13} \text{ cm}^2 \text{ s}^{-1}$ . This difference in diffusion coefficients can be well explained by the result of the topological analysis showing that the fourfold rings in LLNO are more favorable for  $\text{Li}^+$  diffusion than those in  $\text{TiNb}_2\text{O}_7$ . Furthermore, such a tendency of  $\text{Li}^+$  diffusion with respect to the shape of fourfold ring is consistent with discussions in previous studies on LLNO.<sup>6,13)</sup> Therefore, the results demonstrate that the topological analyses based on PH performed in this study are effective for elucidating the relationship between ionic diffusion and atomic configuration in perovskite-related compounds. As an extension, systematic investigations of various perovskite-related materials are expected to lead to the design of corner-sharing octahedral networks suitable for ion conduction.

#### 4. Conclusions

The atomic configuration of LLNO with an A-site-deficient perovskite structure was constructed herein via RMC modeling employing total scattering data. The polyhedral volumes of  $\text{LaO}_{12}$  suggest that the incorporation of La into the La-poor layer changed the volume of the layer and then facilitated  $\text{Li}^+$  diffusion across the layer. In addition, the size of the bottleneck for  $\text{Li}^+$  diffusion in LLNO was successfully evaluated via topological analysis based on PH, and a large bottleneck was suggested as the reason for superior  $\text{Li}^+$  diffusion. Systematic studies of various perovskite-related materials in the future will enable us to uncover corner-sharing octahedral networks suitable for ion conduction.

**Acknowledgments** This research was financially supported by the JSPS Grant-in-Aid for Transformative Research Areas (A) “Hyper-Ordered Structures Science” (Grant Nos. 20H05880, 20H05881, and 20H05884) and JSPS KAKENHI (Grant No. 19KK0068). We are grateful to Dr. K. Osaka (JASRI) for his support with the X-ray diffraction measurements at SPring-8, Japan (Proposal No. 2019B1882). We thank Dr. T. Honda (KEK) for his support of with neutron total scattering measurement conducted at J-PARC, Japan (Proposal No. 2024A0180).

#### References

- 1) D. Larcher and J.-M. Tarascon, *Nat. Chem.* 7, 19 (2015).
- 2) M. S. Whittingham, *MRS Bull.* 33, 411 (2008).
- 3) Y. Kawakami, H. Ikuta and M. Wakihara, *J. Solid State Electr.* 2, 206 (1998).
- 4) S. García-Martín, J. M. Rojo, H. Tsukamoto, E. Morán and M. A. Alario-Franco, *Solid State Ionics* 116, 11 (1999).
- 5) A. Belous, E. Pashkova, O. Gavrilenko, O. V'yunov and L. Kovalenko, *J. Eur. Ceram. Soc.* 24, 1301 (2004).
- 6) X. Gao, C. A. J. Fisher, Y. H. Ikuhara, Y. Fujiwara, S. Kobayashi, H. Moriwake, A. Kuwabara, K. Hoshikawa, K. Kohama, H. Iba and Y. Ikuhara, *J. Mater. Chem. A* 3, 3351 (2015).
- 7) Y. Fujiwara, K. Hoshikawa and K. Kohama, *J. Cryst. Growth* 433, 48 (2016).
- 8) X. Hu, C. A. J. Fisher, S. Kobayashi, Y. H. Ikuhara, Y. Fujiwara, K. Hoshikawa, H. Moriwake, K. Kohama, H. Iba and Y. Ikuhara, *Acta Mater.* 156, 379 (2018).
- 9) Md. S. Ali, Y. Maruyama, M. Nagao, S. Watauchi and I. Tanaka, *Solid State Ionics* 350, 115330 (2020).
- 10) S. Minegishi, T. Hoshina, T. Tsurumi, K. Lebbou and H. Takeda, *J. Ceram. Soc. Jpn.* 128, 481 (2020).
- 11) Z. Yang, R. E. Ward, N. Tanibata, H. Takeda, M. Nakayama and T. Asaka, *J. Phys. Chem. C* 124, 9746 (2020).
- 12) J. Hong, S. Kobayashi, A. Kuwabara, Y. H. Ikuhara, Y. Fujiwara and Y. Ikuhara, *Molecules* 26, 3559 (2021).
- 13) Z. Yang, R. E. Ward, N. Tanibata, H. Takeda, M. Nakayama and R. Kobayashi, *Solid State Ionics* 336–367, 115662 (2021).
- 14) Y. Sakai, D. Urushihara, T. Asaka, K. Fukuda, Z. Yang, N. Tanibata, H. Takeda and M. Nakayama, *Phys. Status Solidi B* 259, 2100561 (2022).
- 15) M. Nakayama, K. Imaki, H. Ikuta, Y. Uchimoto and M. Wakihara, *J. Phys. Chem. B* 106, 6437 (2002).
- 16) X. Xiong, L. Yang, G. Liang, C. Wang, G. Chen, Z. Yang and R. Che, *Adv. Funct. Mater.* 32, 2106911 (2022).
- 17) K. Hayashi, N. Happon, S. Hosokawa, W. Hu and T. Matsushita, *J. Phys.-Condens. Mat.* 24, 093201 (2012).
- 18) K. Kimura, *J. Phys. Soc. Jpn.* 91, 091005 (2022).
- 19) K. Kimura, S. Yamazaki, N. Kitamura, Y. Takabayashi, H. Takeda, R. Kobayashi, H. Tajiri, T. Honda and K. Hayashi, *J. Appl. Phys.* 138, 115109 (2025).
- 20) R. L. McGreevy and L. Pusztai, *Mol. Simulat.* 1, 359 (1988).
- 21) N. Kitamura and S. Kohara, in “Hyperordered Structures in Materials: Disorder in Order and Order within Disorder”, Ed. by K. Hayashi, Chap. 10, Springer (2023) pp. 249–263.
- 22) J.-T. Han, Y.-H. Huang and J. B. Goodenough, *Chem. Mater.* 23, 2027 (2011).
- 23) K. Ise, S. Morimoto, Y. Harada and N. Takami, *Solid State Ionics* 320, 7 (2018).
- 24) R. Inada, R. R. Kumasaka, S. Inabe, T. Tojo and Y. Sakurai, *J. Electrochem. Soc.* 166, A5157 (2019).
- 25) K. J. Griffith, I. D. Seymour, M. A. Hope, M. M. Butala, L. K. Lamontagne, M. B. Preefer, C. P. Koçer, G. Henkelman, A. J. Morris, M. J. Cliffe, S. E. Dutton and C. P. Grey, *J. Am. Chem. Soc.* 141, 16706 (2019).
- 26) N. Kitamura, H. Matsubara, K. Kimura, I. Obayashi, Y.

- Onodera, K. Nakashima, H. Morita, M. Shiga, Y. Harada, C. Ishibashi, Y. Idemoto and K. Hayashi, *NPG Asia Mater.* **16**, 62 (2024).
- 27) F. Izumi and K. Momma, *Solid State Phenom.* **130**, 15 (2007).
- 28) D. A. Keen, *J. Appl. Crystallogr.* **34**, 172 (2001).
- 29) M. G. Tucker, D. A. Keen, M. T. Dove, A. L. Goodwin and Q. Hui, *J. Phys.-Condens. Mat.* **19**, 335218 (2007).
- 30) I. D. Brown and D. Altermatt, *Acta Crystallogr. B* **41**, 244 (1985).
- 31) S. T. Norberg, M. G. Tucker and S. Hull, *J. Appl. Crystallogr.* **42**, 179 (2009).
- 32) <https://shinichinishimura.github.io/pyabst/>.
- 33) S. Le Roux and P. Jund, *Comp. Mater. Sci.* **49**, 70 (2010).
- 34) I. Obayashi, T. Nakamura and Y. Hiraoka, *J. Phys. Soc. Jpn.* **91**, 091013 (2022).
- 35) <https://homcloud.dev/index.en.html>.
- 36) Y. Hiraoka, T. Nakamura, A. Hirata, E. G. Escobar, K. Matsue and Y. Nishiura, *P. Natl. Acad. Sci. USA* **113**, 7035 (2016).
- 37) N. Kitamura, R. Nagai, C. Ishibashi and Y. Idemoto, *Electrochemistry* **92**, 087002 (2024).
- 38) N. Kitamura, Y. Suzuki, C. Ishibashi and Y. Idemoto, *Electrochemistry* **93**, 063010 (2025).
- 39) C. S. Mariani and L. W. Hobbs, *J. Non-Cryst. Solids* **124**, 242 (1990).
- 40) F. Yu, S. Wang, R. Yekani, A. L. Monaca and G. P. Demopoulos, *J. Energy Storage* **95**, 112482 (2024).